ACS APPLIED MATERIALS & INTERFACES
Research Article
www.acsami.org

Relevance between the Bulk Density and Li^+-Ion Conductivity in a Porous Electrolyte: The Case of $Li[Li_{1/3}Ti_{5/3}]O_4$

Kazuhiko Mukai,* Naoyoshi Nunotani,† and Ryuta Moriyasu

Toyota Central Research and Development Laboratories, Inc., 41-1 Yokomichi, Nagakute, Aichi 480-1192, Japan

Supporting Information

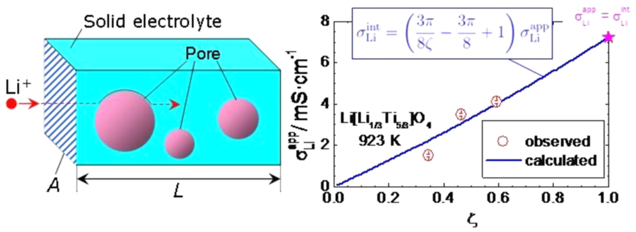

ABSTRACT: The Li^+-ion conductivity (σ_{Li}) in an electrolyte is an important parameter with respect to the performance of all-solid-state lithium-ion batteries (LIBs). However, little is known about how σ_{Li} in a porous electrolyte differs from that in a highly dense electrolyte. In this study, the relationship between the bulk density (d_{bulk}) and apparent σ_{Li} (σ_{Li}^{app}) in a porous electrolyte of $Li[Li_{1/3}Ti_{5/3}]O_4$ (LTO) was examined by theoretical and experimental approaches. The theoretical calculations demonstrated that d_{bulk} and σ_{Li} have a simple relationship irrespective of the radius of the spherical pores in the electrolyte; i.e., σ_{Li} increases almost linearly with increasing ζ, where ζ is the ratio of d_{bulk} to the theoretical density. In fact, the observed σ_{Li}^{app} of LTO, which was determined by four-probe alternating-current impedance measurements, increased with increasing ζ. Hence, with this relationship, σ_{Li}^{app} can be estimated by ζ and intrinsic σ_{Li} (σ_{Li}^{int}) and vice versa; such estimations provide critical information for determining the optimum compositions of composite electrodes for all-solid-state LIBs. The temperature dependence of σ_{Li}^{app} in LTO and differences between the calculated and experimental results are also discussed.

KEYWORDS: *lithium titanium oxide, spinel, lithium-ion battery, solid electrolyte, impedance measurements*

1. INTRODUCTION

The concept of “local production for local consumption” originated in regional communities that produce agricultural and/or marine products. Recently, because of the depletion of resources, this concept has expanded to the field of energy resources; i.e., electricity generated by renewable and sustainable energy is consumed as locally as possible. To realize such a concept, one of the most challenging tasks is the production of all-solid-state lithium-ion batteries (LIBs) with high energy and power densities.[1] All-solid-state LIBs contain a solid electrolyte, instead of the organic liquid electrolyte that is currently used in conventional LIBs.

Solid electrolytes such as $Li_{3x}La_{2/3-x}TiO_3$[2] and $Li_7La_3Zr_2O_{12}$[3] are usually synthesized at temperatures (T) above 1300 K to obtain a highly dense solid electrolyte. Conversely, electrode materials such as $LiCoO_2$[4] and $Li[Li_{1/3}Ti_{5/3}]O_4$ (LTO)[5−7] are usually synthesized at $T \leq 1023$ K. Note that LTO is considered to be an ideal electrode material for all-solid-state LIBs because the change in its lattice parameter ($a_c \simeq 8.36$ Å) during charge and discharge reactions is negligibly small.[5,6] The difference in the synthesis T between solid electrolytes and electrode materials makes it difficult to achieve well-connected interfaces by sintering these compounds in a body. The situation is similar to that of solid oxide fuel cells, which requires knowledge of the sintering and thermal behavior of the various components.[8] Consequently, the solid electrolytes in actual all-solid-state LIBs are more porous than those prepared at higher T. Therefore, the effects of a porous electrolyte structure and/or its bulk density (d_{bulk}) on Li^+-ion conductivity (σ_{Li}) should be clarified to facilitate the further development of all-solid-state LIBs.

In this study, we investigated the relevance between σ_{Li} and d_{bulk} in LTO using theoretical as well as experimental approaches. One of the reasons for our interest in this material is its potential application in all-solid-state LIBs, as previously mentioned. Another reason is that the nature of σ_{Li} in as-synthesized LTO has not been fully elucidated probably because of differences in the structure and/or d_{bulk} between porous and nonporous electrolytes. For example, the reported activation energies (E_a) for σ_{Li} in LTO range from 0.42 to 0.94 eV even though these values were calculated from data collected over similar T ranges.[9−15] Furthermore, the plots of log σ_{Li} versus $1/T$ have been reported to contain one or two slope changes,[9−12] whereas other authors[13−15] have reported a linear $1/T$ dependence on σ_{Li}.

We used theoretical calculations to reveal how spherical pores in an electrolyte influence its apparent σ_{Li} (σ_{Li}^{app}). We then performed alternating-current (ac) impedance measurements to examine σ_{Li} for LTOs with three different d_{bulk} values and compared the results with those of the calculations. The LTO samples were prepared by a combination of preheating (PH) and cold isostatic pressing (CIP) methods. The PH method, which consists of a heat treatment at 673 K, is effective for eliminating closed pores in an LTO pellet, whereas the CIP

Received: July 2, 2015
Accepted: August 25, 2015
Published: August 25, 2015

DOI: 10.1021/acsami.5b05952
ACS Appl. Mater. Interfaces 2015, 7, 20314−20321

method provides greater compression compared to the conventional uniaxial pressing (UP) method. Here, heating at $T \geq 1123$ K was observed to result in an Li_2TiO_3 impurity in LTO, which significantly degrades the electrochemical properties of LTO.[5,6] Thus, we restricted the synthesis T to 1023 K to obtain single-phase LTO. Moreover, we used a four-probe ac impedance method because, in principle, it detects only two impedance components: a bulk impedance and a grain-boundary impedance.

2. EXPERIMENTAL SECTION

The pelletized LTO samples were prepared via a solid-state reaction technique using $LiOH{\cdot}H_2O$ and TiO_2 anatase powders (Wako Pure Chemical Industries, Ltd.), as reported previously.[6,7] The powders were mixed in an Li/Ti molar ratio of 4.08/5 and then pressed into a pellet with diameter and thickness of ~23 and ~5 mm, respectively. The pellet was heated at 1023 K for 12 h under flowing oxygen. Hereafter, we denote this LTO sample as LTO(UP) because it was compacted at 20 MPa for 1 min using the UP method. We also used two other procedures: the CIP method and a combination of the PH and CIP methods. In the case of the LTO(CIP) sample, the pellet was pressed at 200 MPa for 3 min, followed by UP at 20 MPa. During CIP, the pellet was packed into a nylon bag to avoid an undesirable reaction with water. For the LTO(PH+CIP) sample, the pellet was preheated at 673 K for 12 h under flowing oxygen. The obtained pellets were finally sintered at 1023 K for 12 h under flowing oxygen, as in the case of the LTO(UP) sample. In the case of the LTO(PH+CIP) sample, we examined the heating T dependence on d_{bulk}. After the PH and CIP treatments, the LTO pellet was heated at 1123, 1223, or 1323 K under flowing oxygen; these samples are represented as LTO(PH+CIP,1123K), LTO(PH+CIP,1223K), and LTO(PH+CIP,1323K), respectively.

We characterized the crystal structures and electrochemical properties of the LTO(UP), LTO(CIP), LTO(PH+CIP), LTO(PH+CIP,1123K), LTO(PH+CIP,1223K), and LTO(PH+CIP,1323K) samples. X-ray diffraction (XRD) data were collected by a step scanning method in the 2θ range from 15 to 140° using Fe $K\alpha$ radiation (D8 ADVANCE, Bruker AXS, Inc.). Structural parameters such as the cubic lattice (a_c) and oxygen (u) parameters were determined by Rietveld analysis using the *RIETAN-FP* software.[16] The electrochemical properties were evaluated in a nonaqueous lithium cell. The electrode, which consisted of 70 wt % LTO powder, 25 wt % acetylene black, and 5 wt % poly(tetrafluoroethylene) binder, was pressed on a copper mesh (⌀ 15 mm). Lithium metal pressed on a stainless steel plate (⌀ 19 mm) was used as the counter electrode. Two sheets of polypropylene porous membrane (TonenGeneral Sekiyu K. K.) were used as the separator. The electrolyte used was 1 M $LiPF_6$ dissolved in an ethylene carbonate/diethyl carbonate (1/1 volume ratio) solution. The cell was assembled in an argon-filled glovebox and was operated at 0.1 mA (~0.056 $mA{\cdot}cm^{-2}$) from 1.0 to 3.0 V at 298 K. Nitrogen adsorption and desorption isotherms were measured for the powdered LTO(UP) and LTO(PH+CIP) samples at 77 K (AUTOSORB-1, Quantachrome Instruments Inc.). Brunauer–Emmett–Teller (BET) surface areas were determined by the linear part of the BET plot in the P/P_0 range between 0.1 and 0.3.

The σ_{Li} values for the LTO(UP), LTO(CIP), and LTO(PH+CIP) samples were determined from the results of the four-probe ac impedance measurements. A pellet was cut from each of the three samples and then polished with waterproof abrasive papers. The dimensions ($H \times W \times D$) of the LTO(UP), LTO(CIP), and LTO(PH+CIP) pellets were 3.70(2) × 10.67(2) × 0.80(2) mm^3, 2.65(2) × 12.02(2) × 2.26(2) mm^3, and 5.84(2) × 13.09(2) × 2.38(2) mm^3, respectively. By using these dimensions (volume) and the weight of each sample, we calculated the d_{bulk} values for the LTO(UP), LTO(CIP), and LTO(PH+CIP) samples. Each pellet surface was observed by scanning electron microscopy (SEM; S-3600N, Hitachi High-Technologies Co., Ltd.). After four gold terminals were painted on the pellets with gold paste, the pellets were heated at 923 K to volatilize the organic binders in the paste. The distance between each gold terminal was ~3 mm. The ac impedance measurements (1260 impedance/gain phase analyzer, Solartron) were conducted in the T range from 923 to 473 K as the samples cooled. The frequency (f) range was 0.1−10 MHz. During the measurements, N_2 gas was flowed over the sample at 500 $mL{\cdot}min^{-1}$.

3. RESULTS

3.1. Theoretical Calculation of $\sigma_{\mathrm{Li}}^{\mathrm{app}}$.

$\sigma_{\mathrm{Li}}^{\mathrm{app}}$ is assumed to be decreased from an intrinsic σ_{Li} ($\sigma_{\mathrm{Li}}^{\mathrm{int}}$) by the presence of pores in an electrolyte. In this section, the relationship between $\sigma_{\mathrm{Li}}^{\mathrm{app}}$ and $\sigma_{\mathrm{Li}}^{\mathrm{int}}$ was examined. Figure 1a shows the schematic of a porous solid electrolyte with a Li^+ ion moving through the electrolyte and dodging numerous pores. For simplicity, we assumed that (i) the solid electrolyte and each pore form rectangular and spherical shapes, respectively, (ii) a Li^+ ion moves straight unless it encounters spherical pores, and (iii) each spherical pore exists separately in the electrolyte. Here, A is the surface area of the side of the electrolyte, L is the geometrical length of the solid electrolyte, R is the radius of a spherical pore, and n is the number of spherical pores in the electrolyte. As is evident in Figure 1b, if a Li^+ ion encounters a pore at point P, it should take an indirect path from point P to point P′ to avoid the spherical pore. The direct distance between P and P′ in the spherical pore (l) is given by

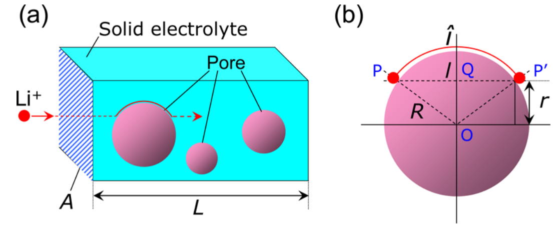

Figure 1. Schematics of (a) a solid electrolyte with spherical pores and (b) a circuitous path around the spherical pore for Li^+-ion conduction. A is the surface area of the side of a rectangular solid electrolyte, and L is its geometrical length. l is the direct distance from point P to point P′, whereas $\hat{l}$ is the detour distance from P to P′ around the spherical pore. R is the spherical pore radius in the electrolyte, and r is the distance between points Q and O.

$$l = 2\sqrt{R^2 - r^2} \tag{1}$$

whereas the detour distance from P to P′ around the spherical pore ($\hat{l}$) is represented by

$$\hat{l} = 2R \arccos(r/R) \tag{2}$$

where r is the distance between points O and Q in Figure 1b. Thus, the average difference between l and $\hat{l}$ ($\overline{\Delta l}$) is determined by using a line integral function $\int_C$,

$$\overline{\Delta l} = \int_0^R \int_C \Delta l \ \mathrm{d}C \ \mathrm{d}r / \pi R^2 \tag{3}$$

where C is the integral region of the circle, the radius of which is r. Note that $\overline{\Delta l}$ averages all of the Li^+ ions that encounter the spherical pore. Because $\int_C \Delta l \ \mathrm{d}C = 2\pi r \Delta l$, $\overline{\Delta l}$ is calculated as

$$\begin{aligned}\overline{\Delta l} &= \int_0^R 2\pi r\left(2R\arccos\frac{r}{R} - 2\sqrt{R^2-r^2}\right)\mathrm{d}r/\pi R^2\\ &= \frac{4}{R}\int_0^R r\arccos\frac{r}{R}\,\mathrm{d}r - \frac{4}{R^2}\int_0^R r\sqrt{R^2-r^2}\,\mathrm{d}r\\ &= \frac{4}{R}\left[\frac{1}{4}R^2\arccos\frac{r}{R}\left(\frac{2r^2}{R^2}-1\right) - \frac{1}{4}rR\sqrt{1-\frac{r^2}{R^2}}\right]_0^R\\ &\quad - \frac{4}{R^2}\left[-\frac{1}{3}(R^2-r^2)^{3/2}\right]_0^R\\ &= \left(\frac{\pi}{2}-\frac{4}{3}\right)R \end{aligned} \tag{4}$$

The total detour distance in the solid electrolyte $(\overline{\Delta L})$ is represented as

$$\overline{\Delta L} = \pi R^2 n\overline{\Delta l}/A = \left(\frac{\pi}{2}-\frac{4}{3}\right)\frac{\pi n R^3}{A} \tag{5}$$

Therefore, the effective distance of Li^+-ion conduction in the porous electrolyte (L_{eff}) is given by

$$L_{\mathrm{eff}} = L + \overline{\Delta L} = L + \left(\frac{\pi}{2}-\frac{4}{3}\right)\frac{\pi n R^3}{A} \tag{6}$$

Here, the ratio of d_{bulk} to the theoretical density, i.e., the density determined by an XRD measurement (d_{XRD}), is calculated using the spherical pore volume V_{pore} $(=4/3\pi n R^3)$, i.e.,

$$d_{\mathrm{bulk}}/d_{\mathrm{XRD}} = (LA - V_{\mathrm{pore}})/LA = 1 - \frac{4}{3}\frac{\pi n R^3}{LA} \tag{7}$$

Applying $d_{\mathrm{bulk}}/d_{\mathrm{XRD}} \equiv \zeta$, we rewrite L_{eff} as

$$L_{\mathrm{eff}} = L\left[\frac{3\pi}{8} - \left(\frac{3\pi}{8}-1\right)\zeta\right] \tag{8}$$

However, the total surface area of spherical pores (A_{pore}) is equal to the decrease in the average surface area $(\overline{\Delta A})$ when a Li^+ ion takes an alternate path to avoid spherical pores. Hence, $\overline{\Delta A}$ is obtained by

$$\overline{\Delta A} = \frac{4}{3}\frac{\pi n R^3}{L} \tag{9}$$

The effective surface area for Li^+-ion conduction (A_{eff}) is thus given by

$$A_{\mathrm{eff}} = A - \overline{\Delta A} = A\zeta \tag{10}$$

Here, $\sigma_{\mathrm{Li}}^{\mathrm{app}}$ has the following relationship with $\sigma_{\mathrm{Li}}^{\mathrm{int}}$:

$$\sigma_{\mathrm{Li}}^{\mathrm{app}} = \frac{L}{L_{\mathrm{eff}}}\frac{A_{\mathrm{eff}}}{A}\sigma_{\mathrm{Li}}^{\mathrm{int}} \tag{11}$$

Using eqs 6 and 10, we determine the ratio of $\sigma_{\mathrm{Li}}^{\mathrm{app}}$ to $\sigma_{\mathrm{Li}}^{\mathrm{int}}$ by

$$\frac{L}{L_{\mathrm{eff}}}\frac{A_{\mathrm{eff}}}{A} = \frac{1}{\frac{3\pi}{8\zeta} - \frac{3\pi}{8} + 1} \tag{12}$$

As clearly shown in eq 12, $\sigma_{\mathrm{Li}}^{\mathrm{app}}$ depends only on ζ, indicating that the size of the pores (R or r) does not influence $\sigma_{\mathrm{Li}}^{\mathrm{app}}$.

Parts a and b of Figure 2 show the ζ dependence of (a) L_{eff}/L and (b) $\sigma_{\mathrm{Li}}^{\mathrm{app}}/\sigma_{\mathrm{Li}}^{\mathrm{int}}$, respectively. As ζ increases from 0 to 1, L_{eff}/L decreases linearly from ~1.18 to 1. Almost a one-to-one relationship is observed between ζ and $\sigma_{\mathrm{Li}}^{\mathrm{app}}/\sigma_{\mathrm{Li}}^{\mathrm{int}}$, but strictly speaking, the ζ dependence of $\sigma_{\mathrm{Li}}^{\mathrm{app}}/\sigma_{\mathrm{Li}}^{\mathrm{int}}$ is not linear with ζ. That is, when $\zeta = 0.5$, $\sigma_{\mathrm{Li}}^{\mathrm{app}}/\sigma_{\mathrm{Li}}^{\mathrm{int}}$ is slightly less than 0.5.

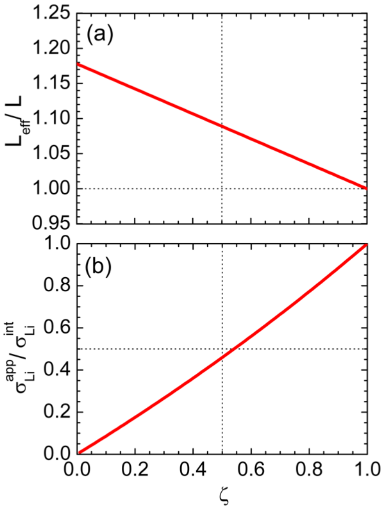

Figure 2. Theoretical (a) L_{eff}/L and (b) $\sigma_{\mathrm{Li}}^{\mathrm{app}}/\sigma_{\mathrm{Li}}^{\mathrm{int}}$ values as a function of ζ. The former was calculated by eq 8 and the latter by eqs 11 and 12.

3.2. Characterization. Before measuring σ_{Li} of the LTO samples, we first characterized their structural and electrochemical properties. As per previous studies,[5−7,11,13] LTO is known to crystallize in a spinel structure with space group $Fd\bar{3}m$, in which Li^+ ions occupy tetrahedral 8a and octahedral 16d sites, whereas Ti^{4+} ions occupy the octahedral 16d site. As is evident in Figure S1 of the Supporting Information, the XRD patterns for the LTO(CIP) and LTO(PH+CIP) samples were indexed as single-phase spinel structures. Conversely, the XRD pattern for the LTO(UP) sample was indexed as a mixture of the spinel structure and TiO_2 anatase because a small diffraction peak due to the (101) plane of TiO_2 anatase was observed at $2\theta \simeq 32°$. Except for the existence of TiO_2 anatase, the structural parameters for the present LTO samples are in good agreement with previously reported values,[5−7] as listed in Table S1 of the Supporting Information.

Figure 3 shows the charge/discharge curves of the electrochemical cells containing the (a) LTO(UP), (b) LTO(CIP), and (c) LTO(PH+CIP) samples. Note that electrochemical charge/discharge tests are the best method for characterizing LTO, although the present study is focused on their performance as an electrolyte, not as an electrode. In the cases of all of the samples, the operating voltage rapidly decreases to ~1.6 V from ~3.2 V versus Li^+/Li during the initial discharge reaction. The discharge capacities (Q_{dis}) are ~169 mAh·g^{-1}, which is ~96% of the theoretical capacity (175 mAh·g^{-1}) of LTO based on the following reaction:

$$Li[Li_{1/3}Ti_{5/3}]O_4 + Li^+ + e^- \leftrightarrow Li_2[Li_{1/3}Ti_{5/3}]O_4 \tag{13}$$

However, the subsequent charge/discharge curves of the three samples differ. The irreversible capacity (Q_{irre}) at the initial cycle is greater than 11 mAh·g^{-1} for the LTO(UP) and LTO(CIP) samples, whereas Q_{irre} is ~4 mAh·g^{-1} for the LTO(PH+CIP) sample. Moreover, in the cases of the LTO(UP) and LTO(CIP) samples, the redox reaction associated with TiO_2 anatase is observed at ~2.0 V,[17] indicating that these samples contain mixtures of LTO and TiO_2 anatase. Because no trace of TiO_2 anatase was observed in the XRD pattern of the LTO(CIP) sample (Figure S1b), the electro-

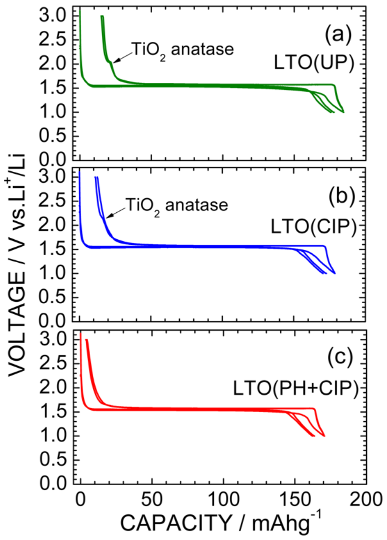

Figure 3. Charge and discharge curves of the Li/LTO cells containing (a) LTO(UP), (b) LTO(CIP), and (c) LTO(PH+CIP). The cells were cycled at 298 K at a current density of 0.056 mA·cm^{-2} in the voltage range of 1.0−3.0 V.

chemical charge/discharge tests are more sensitive than conventional XRD measurements.

As listed in Table 1, d_{bulk} for LTO(UP) is 1.20(1) g·cm^{-3}, which is ∼34% of d_{XRD} for the ideal LTO (=3.48 g·cm^{-3}). The d_{bulk} value is increased by the CIP and PH methods; i.e., d_{bulk} = 1.62(1) g·cm^{-3} for LTO(CIP) and d_{bulk} = 2.07(1) g·cm^{-3} for LTO(PH+CIP); however, even in the case of LTO(PH+CIP), ζ (=$d_{\mathrm{bulk}}/d_{\mathrm{XRD}}$) is limited to 0.595(5). Although this ζ is substantially smaller than those of typical solid electrolytes (>0.9),[2,3] we expect that increasing ζ of LTO beyond this value would be difficult. To obtain a highly dense compound, sintering at high T would be effective. In fact, the d_{bulk} values for the LTO(PH+CIP,1123K), LTO(PH+CIP,1223K), and LTO(PH+CIP,1323K) samples were increased to 2.60(1), 2.98(1), and 2.90(1) g·cm^{-3}, respectively. However, as shown in Figure S2 of the Supporting Information, a diffraction line due to a Li_2TiO_3 phase is observed in the XRD patterns of the LTO(PH+CIP,1223K) and LTO(PH+CIP,1323K) samples. Furthermore, the high T synthesis above 1023 K and/or the presence of the Li_2TiO_3 phase decreases Q_{dis} for LTO; Q_{dis} = 150 mAh·g^{-1} for LTO(PH+CIP,1123K), Q_{dis} = 110 mAh·g^{-1} for LTO(PH+CIP,1223K), and Q_{dis} = 130 mAh·g^{-1} for LTO(PH+CIP,1323K) (see Figure S3 of the Supporting Information). This confirms that these samples are no longer single-phase LTO but contain electrochemical inactive phases such as Li_2TiO_3. This situation is similar to that for the nominal composition compound $Li[Li_{1/3}Mn_{5/3}]O_4$, which contains a small amount of the Li_2MnO_3 phase.[18] Thus, we restricted our ac impedance measurements to single-phase LTO, i.e., the LTO(UP), LTO(CIP), and LTO(PH+CIP) samples that were prepared at 1023 K.

3.3. SEM Images.

Figure 4 displays the SEM images of the three LTO samples for clarification of their structures. The LTO(UP) sample surface appears to be flat and dense at the 100 μm scale (Figure 4a); however, primary particles with an average size of ∼0.4 μm are still observed to be separated from each other at the 1 μm scale (Figure 4d). This observation indicates that the LTO(UP) sample contains numerous microsized pores with diameters from 0.1 to 1 μm. In contrast, in the SEM micrographs of the LTO(CIP) and LTO(PH+CIP) samples, shown in parts e and f of Figure 4, respectively, clearances or grain boundaries between primary particles are hardly observed at the 1 μm scale. This result suggests that the CIP method is useful for eliminating microsized pores in the sample, although there is a possibility that microsized pores still exist in the bulk of the sample.

Unpredictably, macrosized pores with diameters from 50 to 100 μm are observed on the LTO(CIP) and LTO(PH+CIP) surfaces (parts b and c of Figure 4, respectively). The number of macrosized pores in the LTO(PH+CIP) sample is considerably smaller than that in the LTO(CIP) sample. Such macrosized pores are considered to be caused by a dehydration reaction of $LiOH·H_2O$ as follows. When the heating T reaches 450−600 K, the crystallization water of $LiOH·H_2O$ begins to evaporate from the LTO pellets. Because the primary particles in the LTO(CIP) sample stick to each other, evaporation of water produces macrosized pores on the surface. In the case of the LTO(PH+CIP) sample, the PH procedure, i.e., the regrinding and repressing of the pellet before the final-stage sintering at 1023 K, effectively decreases the occurrence of macrosized pores. In addition, in the case of the LTO(UP) sample, the presence of microsized pores facilitates water evaporation; consequently, few macrosized pores are formed when the PH procedure is not used. Therefore, both the CIP and the PH methods increased d_{bulk} of the LTO pellet by decreasing the occurrence of microsized and macrosized pores, respectively.

Although the resolution of SEM observations is limited, nanosized pores with diameters below 0.1 μm are expected to exist in the LTO samples because the high T syntheses above 1023 K result in greater d_{bulk} values. Here, d_{XRD} of Li_2TiO_3 is calculated to be 3.29 g·cm^{-3},[6] which is slightly smaller than that of LTO (=3.48 g·cm^{-3}). Therefore, the increase in d_{bulk} for LTO(PH+CIP,1123K) and LTO(PH+CIP,1223K) is attributed to the elimination of nanosized pores, whereas the slight decrease in d_{bulk} for LTO(PH+CIP,1323K) is caused by the formation of Li_2TiO_3.

The BET surface areas for the powdered LTO(UP) and LTO(PH+CIP) samples were 5.0 and 4.7 m^2·g^{-1}, respectively. This indicates that the average size of aggregated secondary

Table 1. Bulk Density (d_{bulk}), Ratio of d_{bulk} to the XRD Density ($\zeta = d_{\mathrm{bulk}}/d_{\mathrm{XRD}}$), and the Results of the Four-Probe ac Impedance Measurements for the LTO(UP), LTO(CIP), and LTO(PH+CIP) Samples

sample	d_{bulk}/g·cm^{-3}	ζ[a]	$\sigma_{\mathrm{Li}}^{\mathrm{app}}$(923 K)/mS·cm^{-1}	E_a/eV 923−773 K	E_a/eV 748−573 K
LTO(UP)	1.20(1)	0.345(8)	1.50(7)	0.66(5)	0.57(5)
LTO(CIP)	1.62(1)	0.465(6)	3.48(6)	0.69(4)	0.49(4)
LTO(PH+CIP)	2.07(1)	0.595(5)	4.10(6)	0.69(4)	0.59(4)

[a] The d_{XRD} values of LTO and Li_2TiO_3 are 3.48 and 3.29 g·cm^{-3}, respectively.

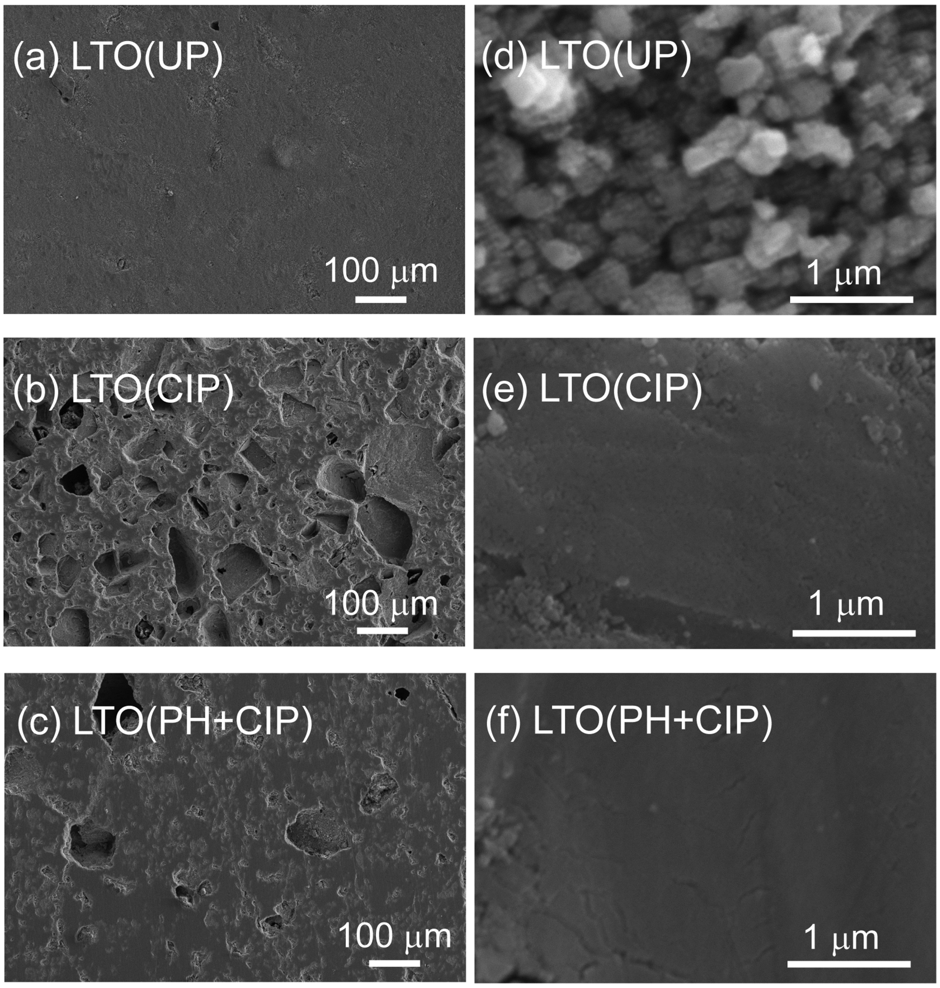

Figure 4. SEM images of the surfaces of the (a) LTO(UP), (b) LTO(CIP), and (c) LTO(PH+CIP) pellets at the 100 μm scale. Their corresponding magnified images at the 1 μm scale are also shown in parts d−f, respectively.

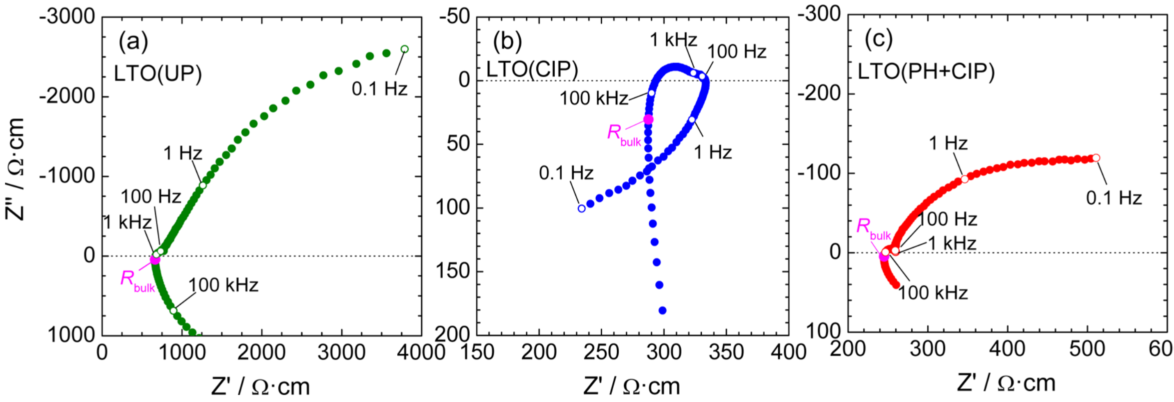

Figure 5. Cole−Cole plots for the (a) LTO(UP), (b) LTO(CIP), and (c) LTO(PH+CIP) samples at 923 K. The bulk resistance (R_{bulk}) is calculated by $\sqrt{Z'^2 + Z''^2}$ at the frequencies indicated by the closed circles.

particles of LTO is not so different between samples. Note that these two values are almost consistent with the reported BET surface area of LTO (=5.2 $\text{m}^2 \cdot \text{g}^{-1}$), which was prepared by a conventional solid-state reaction technique.[19]

3.4. ac Impedance Measurements. Ideally, only two semicircles representing the bulk impedance in the high-f range and the grain-boundary impedance in the low-f range should be observed in the four-probe ac impedance spectra. However, at least two parasitic inductance contributions were observed in the actual ac impedance spectra over the entire investigated T range. As an example, Figure 5 shows the Cole−Cole plots at 923 K for the (a) LTO(UP), (b) LTO(CIP), and (c) LTO(PH+CIP) samples. The parasitic inductance is observed in the spectra of both the LTO(CIP) and LTO(PH+CIP) samples at $f \geq 100$ kHz; however, in the spectrum of the LTO(CIP) sample, another parasitic inductance is observed at $f \leq 10$ Hz.

We investigated the electrical noise at 923 K by measuring the impedance spectrum of a gold rod with diameter and length of 0.49 and 6.12 mm, respectively, and observed the parasitic inductance at $f \geq 10$ kHz. Even if we ignore such parasitic inductance, the impedance spectra still comprise at least nine components. Thus, determining the bulk resistance (R_{bulk}) and grain-boundary resistance (R_{gb}) via fitting of the impedance spectra with equivalent circuit models was difficult. However, because the parasitic inductance at high f shifts impedance spectra toward the bottom side of the imaginary Z' axis, R_{bulk} can be estimated by $\sqrt{Z'^2 + Z''^2}$ using the Z'^2 and Z''^2 values at the frequency that shows the minimum value of $\sqrt{Z'^2 + Z''^2}$ (Figure S4 of the Supporting Information). This method has also been applied in the case of an oxide ion conductor, $Ba_2In_2O_5$, with low d_{bulk} values.[20] Hence, the σ_{Li} ($=\sigma_{\mathrm{Li}}^{\mathrm{app}}$) values of LTO are given by

$$\sigma_{\mathrm{Li}}^{\mathrm{app}} = \frac{1}{R_{\mathrm{bulk}}} \frac{L}{A} \tag{14}$$

In the cases of the LTO(CIP) and LTO(PH+CIP) samples, the Z' and Z'' values at $f = 200$ kHz were selected for calculating R_{bulk}, whereas those at $f = 6$ kHz were selected in the case of the LTO(UP) sample because of the presence of an additional parasitic inductance at $f \geq 1$ kHz (see the arrows in Figure S4 of the Supporting Information). The origins of such parasitic inductance are discussed in section 4.1.

Figure 6 shows the T dependence of $\sigma_{\mathrm{Li}}^{\mathrm{app}}$ for the LTO(UP), LTO(CIP), and LTO(PH+CIP) samples. The $\sigma_{\mathrm{Li}}^{\mathrm{app}}$ value increases with increasing ζ; for instance, $\sigma_{\mathrm{Li}}^{\mathrm{app}}$ at 923 K for LTO(UP), LTO(CIP), and LTO(PH+CIP) is 1.50(7), 3.48(6), and 4.10(6) mS·cm^{-1}, respectively (Table 1). For all of the LTO samples, the T dependence of $\sigma_{\mathrm{Li}}^{\mathrm{app}}$ is not monotonic; the slope change in the log $\sigma_{\mathrm{Li}}^{\mathrm{app}}$ versus $1/T$ curve appears at ~750 K. The E_a values in the T range between 923 and 773 K are ~0.70 eV, whereas those in the T range between 748 and 573 K are 0.49−0.59 eV, suggesting a change in the mechanism of Li$^+$-ion conduction at ~750 K (Table 1). The one inflection T dependence of σ_{Li} in LTO has been previously reported by Hayashi et al., although they reported that the E_a value decreases at $T \geq$ ~720 K.[10]

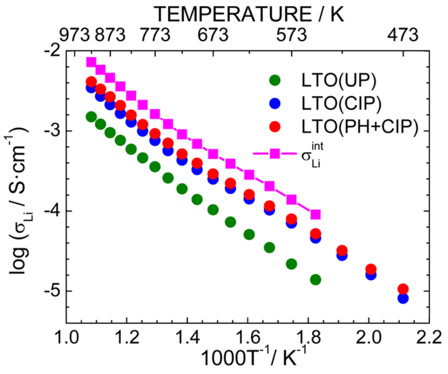

Figure 6. Temperature dependence of the lithium-ion conductivities (σ_{Li}), i.e., the apparent Li$^+$-ion conductivities ($\sigma_{\mathrm{Li}}^{\mathrm{app}}$) for the LTO(UP), LTO(CIP), and LTO(PH+CIP) samples. The intrinsic Li$^+$-ion conductivity ($\sigma_{\mathrm{Li}}^{\mathrm{int}}$) of LTO is also shown for comparison. Note that all σ_{Li} data include error bars.

4. DISCUSSION

4.1. Comparison between the Theoretical and Observed $\sigma_{\mathrm{Li}}^{\mathrm{app}}$ Values. The calculated values of $\sigma_{\mathrm{Li}}^{\mathrm{app}}$ indicate that it increases almost linearly with increasing ζ (Figure 2). To verify this prediction, Figure 7 shows the observed $\sigma_{\mathrm{Li}}^{\mathrm{app}}$ values at (a) 923 K, (b) 748 K, and (c) 548 K as a function of $LA_{\mathrm{eff}}/L_{\mathrm{eff}}A$. Here, the $LA_{\mathrm{eff}}/L_{\mathrm{eff}}A$ values for LTO(UP), LTO(CIP), and LTO(PH+CIP) are calculated to be 0.308(8), 0.424(6), and 0.553(6), respectively, using their ζ values (Table 1). As per eq 11, $\sigma_{\mathrm{Li}}^{\mathrm{app}}$ should increase linearly with a slope of $LA_{\mathrm{eff}}/L_{\mathrm{eff}}A$. In fact, the observed $\sigma_{\mathrm{Li}}^{\mathrm{app}}$ at 923 K increases almost linearly with increasing $LA_{\mathrm{eff}}/L_{\mathrm{eff}}A$. In addition, such a relationship is obtained at 748 and 548 K irrespective of the magnitude of E_a. Thus, the almost linear relationship between $\sigma_{\mathrm{Li}}^{\mathrm{app}}$ and ζ is confirmed by the experimental results, although the range of ζ in this study is restricted to ~0.25; thus, $\sigma_{\mathrm{Li}}^{\mathrm{int}}$ can be estimated from the $\sigma_{\mathrm{Li}}^{\mathrm{app}}$ and ζ values.

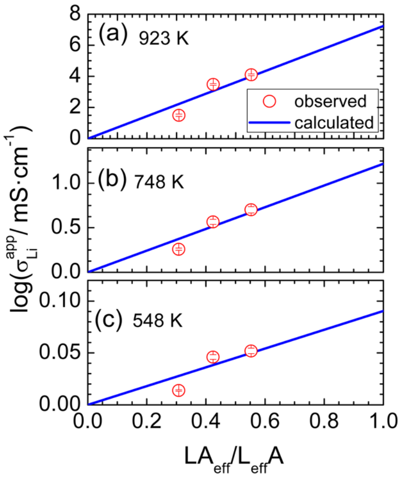

Figure 7. Apparent Li$^+$-ion conductivity ($\sigma_{\mathrm{Li}}^{\mathrm{app}}$) as a function of $LA_{\mathrm{eff}}/L_{\mathrm{eff}}A$ at (a) 923 K, (b) 748 K, and (c) 548 K. The solid circles indicate the observed $\sigma_{\mathrm{Li}}^{\mathrm{app}}$ values. The solid line is the least-squares fitting result for determining the intrinsic Li$^+$-ion conductivity ($\sigma_{\mathrm{Li}}^{\mathrm{int}}$).

As is evident in Figure 7, the observed $\sigma_{\mathrm{Li}}^{\mathrm{app}}$ values at $LA_{\mathrm{eff}}/L_{\mathrm{eff}}A = 0.308$ are slightly lower than the theoretical values. This discrepancy is due to a parasitic inductance caused by microsized pores in the LTO(UP) sample. In the ideal LTO electrolyte, the Li$^+$ ions diffuse in a straightforward manner because of the poreless solid; i.e., $\zeta = 1$. In this electrolyte, no parasitic inductance would be observed, except for contributions from the gold wires and/or the instrument. In contrast, in the case of the LTO(UP) sample with microsized pores, as shown in Figure 4d, the Li$^+$ ions diffuse tortuously to avoid numerous microsized pores in the electrolyte. The L_{eff} value is greater than L (eq 8 or Figure 2a), whereas the A_{eff} value is less than A (eq 10). The tortuous route for Li$^+$-ion conduction naturally generates the parasitic inductance because the radius of the tortuous route, i.e., R, corresponds to the radius of an electromagnetic induction coil. As a result, the presence of microsized pores in the LTO(UP) sample decreases the $\sigma_{\mathrm{Li}}^{\mathrm{app}}$ values.

The situation for the LTO(CIP) sample with macrosized pores is similar to that for the LTO(UP) sample, but its tortuous route differs. In this electrolyte, the Li$^+$ ions must take a longer route to avoid the macrosized pores in the sample (Figure 4b). The differences in the tortuous route affect f of the

DOI: 10.1021/acsami.5b05952
ACS Appl. Mater. Interfaces 2015, 7, 20314−20321

parasitic inductance; the short detour route produces the parasitic inductance in the high-f region, whereas the long detour route produces the parasitic inductance in the low-f region. Consequently, the parasitic inductance at $f \geq 1$ kHz was observed in the impedance spectrum of the LTO(UP) sample, whereas the parasitic inductance at $f \leq 100$ Hz was observed in the spectrum of the LTO(CIP) sample. In the case of the LTO(PH+CIP) sample shown in Figure 5c, the parasitic inductance appeared in the high-f region above 100 kHz. Because the LTO(PH+CIP) sample is almost free of both microsized and macrosized pores at least on the surface, this parasitic inductance arose primarily from the gold wires and the instrument.

As previously described, the observed $\sigma_{\mathrm{Li}}^{\mathrm{app}}$ values increased with increasing $LA_{\mathrm{eff}}/L_{\mathrm{eff}}A$, as expected. However, because of the presence of the parasitic inductance in the high-f region, the observed $\sigma_{\mathrm{Li}}^{\mathrm{app}}$ values for LTO(UP) were slightly lower than the predicted $\sigma_{\mathrm{Li}}^{\mathrm{app}}$ values. This difference indicates that the presence of pores actually influences $\sigma_{\mathrm{Li}}^{\mathrm{app}}$ when their size (R) is on the microscale.

4.2. *T* Dependence of $\sigma_{\mathrm{Li}}^{\mathrm{int}}$ and E_a. The T dependence of $\sigma_{\mathrm{Li}}^{\mathrm{int}}$ of LTO is shown in Figure 6 for comparison with the $\sigma_{\mathrm{Li}}^{\mathrm{app}}$ results for the LTO(UP), LTO(CIP), and LTO(PH+CIP) samples. Here, the $\sigma_{\mathrm{Li}}^{\mathrm{int}}$ value at each T was determined using a least-squares method, as illustrated by the solid line in Figure 7. In the investigated T range, $\sigma_{\mathrm{Li}}^{\mathrm{int}}$ is ~2 times greater than $\sigma_{\mathrm{Li}}^{\mathrm{app}}$ for the LTO(PH+CIP) sample; for instance, $\sigma_{\mathrm{Li}}^{\mathrm{int}}$ at 923 K is 7.4(6) mS·cm^{-1}. A comparison of the present $\sigma_{\mathrm{Li}}^{\mathrm{int}}$ values with the previously reported σ_{Li} values for LTO[9−15] reveals that the present $\sigma_{\mathrm{Li}}^{\mathrm{int}}$ values are similar to the σ_{Li} reported in refs 11 and 12 but slightly larger than the σ_{Li} values reported in refs 9, 14, and 15 (see Figure S5 of the Supporting Information). Note that, however, simple comparisons among σ_{Li} values are difficult because at least two antagonistic factors affect σ_{Li}. That is, a larger ζ value naturally results in a greater σ_{Li} value, whereas the presence of a Li_2TiO_3 phase decreases σ_{Li}.[12] Moreover, ramsdellite-structured $Li_2Ti_3O_7$ exhibits a higher σ_{Li} than that of LTO.[10] Therefore, further studies on LTO, Li_2TiO_3, and $Li_2Ti_3O_7$ with different ζ values would provide critical information for elucidating the σ_{Li} mechanism in LTO.

The $\sigma_{\mathrm{Li}}^{\mathrm{int}}$ versus $1/T$ curve is not monotonic as in the cases for $\sigma_{\mathrm{Li}}^{\mathrm{app}}$ for LTO(UP), LTO(CIP), and LTO(PH+CIP); the E_a at 923−773 K is 0.72(5) eV, whereas the E_a at 748−573 K is 0.49(4) eV. According to Leonidov et al.,[11] LTO exhibits two successive phase transitions of $(\mathrm{Li})_{8a}[\mathrm{Li}_{1/3}\mathrm{Ti}_{5/3}]_{16d}\mathrm{O}_4 \rightarrow [\mathrm{Li}\square]_{16c}[\mathrm{Li}_{1/3}\mathrm{Ti}_{5/3}]_{16d}\mathrm{O}_4 \rightarrow [\mathrm{Li}_{4/3}\square_{2/3}]_{16c}[\square_{1/3}\mathrm{Ti}_{5/3}]_{16d}\mathrm{O}_4$ above 800 K, where 16c is the octahedral site in the $Fd\bar{3}m$ space group. However, no structural phase transitions have been observed in XRD[7] and neutron diffraction[21] patterns collected at temperatures as high as 900 K. Recently, we observed by Raman spectroscopy that the bond interaction between Li and O atoms plays a significant role in determining σ_{Li} of LTO.[7] The T dependence of the E_g band, which corresponds to an asymmetric stretching vibration between Li and O atoms, exhibits a subtle change at approximately 700 K.[7] Hence, the increase in E_a at temperatures above ~750 K is probably due to the local structural change around the LiO_6 octahedra.

4.3. Significance in the LIB Field. Finally, we describe the significance of the present study in the LIB field. Previous studies on solid electrolytes[2,3] appear to have been focused on $\sigma_{\mathrm{Li}}^{\mathrm{int}}$. However, $\sigma_{\mathrm{Li}}^{\mathrm{app}}$ is more important than $\sigma_{\mathrm{Li}}^{\mathrm{int}}$ with respect to the performance in actual all-solid-state LIBs because an electrode usually contains other components such as active material and conducting additives, resulting in lower ζ values. In addition, sintering these compounds in a body at low temperatures decreases ζ. The present findings, in conjunction with the simple relationship described in eqs 11 and 12, indicate the extent to which $\sigma_{\mathrm{Li}}^{\mathrm{int}}$ is decreased in an actual electrolyte and/or electrode. This information could be useful for determining the optimum conditions for fabricating a composite electrode. In contrast, even if $\sigma_{\mathrm{Li}}^{\mathrm{int}}$ is unknown, it can be estimated from the $\sigma_{\mathrm{Li}}^{\mathrm{app}}$ and ζ values, which is an effective approach to exploring advanced solid electrolytes with high $\sigma_{\mathrm{Li}}^{\mathrm{int}}$ values.

As previously discussed, short or long tortuous routes for Li^+-ion conduction generate parasitic inductances in the high-f or low-f regions because of the presence of microsized or macrosized pores in the sample. The fact that macrosized pores rather than microsized pores influence $\sigma_{\mathrm{Li}}^{\mathrm{app}}$ less is critical for controlling the structure of a composite electrode. For instance, examining a combination of an active material and a solid electrolyte with different particle sizes and different particle morphologies would be useful in eliminating microsized pores in an electrolyte and/or electrode.

5. CONCLUSION

The relationship between the bulk density d_{bulk} and the Li^+-ion conductivity σ_{Li} in a porous electrolyte of LTO was examined by theoretical as well as experimental approaches. The theoretical calculations indicated that σ_{Li} ($\sigma_{\mathrm{Li}}^{\mathrm{app}}$) is not influenced by the spherical pore radius but is only dependent on the ratio of d_{bulk} to the theoretical density (ζ); i.e., $\sigma_{\mathrm{Li}}^{\mathrm{app}}$ increases almost linearly with increasing ζ. Here, the theoretical calculation was performed under the assumption that (i) a Li^+ ion moves straight in a rectangular shape of the solid electrolyte unless it encounters spherical pores and (ii) each spherical pore exists separately in the electrolyte. To determine the ζ dependence of $\sigma_{\mathrm{Li}}^{\mathrm{app}}$, we prepared three LTO samples with different ζ values using a combination of the PH and CIP methods. The observed $\sigma_{\mathrm{Li}}^{\mathrm{app}}$ value, which was determined by four-probe ac impedance measurements, increased almost linearly with increasing ζ, as expected. Therefore, the theoretically predicted relationship between $\sigma_{\mathrm{Li}}^{\mathrm{app}}$ and ζ was confirmed by the experimental results, demonstrating that $\sigma_{\mathrm{Li}}^{\mathrm{app}}$ can be estimated by an intrinsic σ_{Li} ($\sigma_{\mathrm{Li}}^{\mathrm{int}}$) and ζ and vice versa. This information could be useful for determining the optimum composition for a composite electrode consisting of active material, solid electrolyte, and conducting additives. The ζ range of the present study was limited to ~0.25 because of the existence of an Li_2TiO_3 impurity phase in LTO. Further studies on other solid electrolytes with larger ζ ranges are underway in our laboratory to elucidate $\sigma_{\mathrm{Li}}^{\mathrm{app}}$ in a porous electrolyte.

■ ASSOCIATED CONTENT

Ⓢ Supporting Information

This material is available free of charge via the Internet at http://pubs.acs.org/. The Supporting Information is available free of charge on the ACS Publications website at DOI: 10.1021/acsami.5b05952.

Results of the Rietveld analyses of the LTO(UP), LTO(CIP), and LTO(PH+CIP) samples, their structural parameters, XRD patterns for the LTO(PH+CIP,1123K), LTO(PH+CIP,1223K), and LTO(PH+CIP,1323K) samples, charge and discharge curves for the LTO(PH+CIP,1123K), LTO(PH+CIP,1223K), and LTO(PH+CIP,1323K) samples, Bode plots for the LTO(UP), LTO(CIP), and LTO(PH+CIP) samples, and T dependence of $\sigma_{\mathrm{Li}}^{\mathrm{int}}$ of LTO, together with the σ_{Li} values that are reported in refs 9−15 (PDF)

AUTHOR INFORMATION

Corresponding Author

*Phone: +81-561-71-7698. Fax: +81-561-63-6948. E-mail: e1089@mosk.tytlabs.co.jp.

Present Address

[†]N.N.: Department of Applied Chemistry, Faculty of Engineering, Osaka University, 2-1 Yamadaoka, Suita, Osaka 565-0871, Japan.

Notes

The authors declare no competing financial interest.

ACKNOWLEDGMENTS

We thank Dr. T. Nakamura for assisting us with the ac impedance measurements and Drs. M. Ohashi and Y. Goto for helping us with the BET surface area measurements. We also thank Dr. S. Morishita and H. Matsuo of TCRDL for their helpful discussions about the ac impedance spectra. K.M. is partially supported by Grant-in-Aid for Scientific Research (C) 25410207 from the Ministry of Education, Culture, Sports, Science and Technology, Japan.

REFERENCES

(1) Masquelier, C. Lithium Ions on the Fast Track. *Nat. Mater.* **2011**, *10*, 649−650.

(2) Stramare, S.; Thangadurai, V.; Weppner, W. Lithium Lanthanum Titanates: A Review. *Chem. Mater.* **2003**, *15*, 3974−3990.

(3) Murugan, R.; Thangadurai, V.; Weppner, W. Fast Lithium Ion Conduction in Garnet-Type $Li_7La_3Zr_2O_{12}$. *Angew. Chem., Int. Ed.* **2007**, *46*, 7778−7781.

(4) Mukai, K.; Kishida, Y.; Nozaki, H.; Dohmae, K. Structural Phase Transition from Rhombohedral ($R\bar{3}m$) to Monoclinic ($C2/m$) Symmetry in Lithium Overstoichiometric $Li_{1+\delta}Co_{1-\delta}O_{2-\delta}$. *Chem. Mater.* **2013**, *25*, 2828−2837.

(5) Ohzuku, T.; Ueda, A.; Yamamoto, N. Zero-Strain Insertion Material of $Li[Li_{1/3}Ti_{5/3}]O_4$ for Rechargable Lithium Cells. *J. Electrochem. Soc.* **1995**, *142*, 1431−1435.

(6) Mukai, K.; Kato, Y.; Nakano, H. Understanding the Zero-Strain Lithium Insertion Scheme of $Li[Li_{1/3}Ti_{5/3}]O_4$: Structural Changes at Atomic Scale Clarified by Raman Spectroscopy. *J. Phys. Chem. C* **2014**, *118*, 2992−2999.

(7) Mukai, K.; Kato, Y. Role of Oxide Ions in Thermally Activated Lithium Diffusion of $Li[Li_{1/3}Ti_{5/3}]O_4$: X-ray Diffraction Measurements and Raman Spectroscopy. *J. Phys. Chem. C* **2015**, *119*, 10273−10281.

(8) Singhal, S. C.; Kendall, K. *High Temperature Solid Oxide Fuel Cells: Fundamentals Design, and Applications*; Elsevier Science: Amsterdam, The Netherlands, 2003.

(9) Fehr, K. T.; Holzapfel, M.; Laumann, A.; Schmidbauer, E. DC and AC Conductivity of $Li_{4/3}Ti_{5/3}O_4$ Spinel. *Solid State Ionics* **2010**, *181*, 1111−1118.

(10) Hayashi, S.; Hatano, H. Ionic Conduction of $Li_2Ti_3O_7$ and $Li_4Ti_5O_{12}$. *Nippon Seramikkusu Kyokai Gakujutsu Ronbunshi* **1994**, *102*, 378−382.

(11) Leonidov, I. A.; Leonidova, O. N.; Perelyaeva, L. A.; Samigullina, R. F.; Kovyazina, S. A.; Patrakeev, M. V. Structure, Ionic Conduction, and Phase Transformations in Lithium Titanate $Li_4Ti_5O_{12}$. *Phys. Solid State* **2003**, *45*, 2183−2188.

(12) Vītiņš, Ģ.; Ķizāne, G.; Lūsis, A.; Tīliks, J. Electrical Conductivity Studies in the System Li_2TiO_3-$Li_{1.33}Ti_{1.67}O_4$. *J. Solid State Electrochem.* **2002**, *6*, 311−319.

(13) Wilkening, M.; Amade, R.; Iwaniak, W.; Heitjans, P. Ultraslow Li Diffusion in Spinel-Type Structured $Li_4Ti_5O_{12}$-A Comparison of Results from Solid State NMR and Impedance Spectroscopy. *Phys. Chem. Chem. Phys.* **2007**, *9*, 1239−1246.

(14) Prosini, P. P.; Mancini, R.; Retrucci, L.; Contini, V.; Villano, P. $Li_4Ti_5O_{12}$ as Anode in All-Solid-State, Plastic, Lithium-Ion Batteries for Low-Power Applications. *Solid State Ionics* **2001**, *144*, 185−192.

(15) Tsubone, D.; Hashimoto, T.; Igarashi, K.; Shimizu, T. Electrical Characterization of Phase Changes in Lithium Titanate. *Nippon Seramikkusu Kyokai Gakujutsu Ronbunshi* **1994**, *102*, 180−184.

(16) Izumi, F.; Momma, K. Three-Dimensional Visualization in Powder Diffraction. *Solid State Phenom.* **2007**, *130*, 15−20.

(17) Ohzuku, T.; Takehara, Z.; Yoshizawa, S. Nonaqueous Lithium/Titanium Dioxide Cell. *Electrochim. Acta* **1979**, *24*, 219−222.

(18) Mukai, K.; Sugiyama, S.; Ikedo, Y.; Nozaki, H.; Kamazawa, K.; Andreica, D.; Amato, A.; MÅnsson, M.; Brewer, J. H.; Ansaldo, E. J.; Chow, K. M. Microscopic Magnetic Study on the Nominal Composition $Li[Li_{1/3}Mn_{5/3}]O_4$ by Muon-Spin Rotation/Relaxation Measurements. *J. Phys. Chem. C* **2010**, *114*, 11320−11327.

(19) Nugroho, A.; Kim, S. J.; Chung, K. Y.; Cho, B.-W.; Lee, Y.-W.; Kim, J. Facile Synthesis of Nanosized $Li_4Ti_5O_{12}$ in Supercritical Water. *Electrochem. Commun.* **2011**, *13*, 650−653.

(20) Jankovic, J.; Wilkinson, D. P.; Hui, R. Electrochemical Impedance Spectroscopy of $Ba_2In_2O_5$: Effect of Porosity, Grain Size, Dopant, Atmosphere, and Temperature. *J. Electrochem. Soc.* **2012**, *159*, B109−B120.

(21) Laumann, A.; Boysen, H.; Bremholm, M.; Fehr, K. T.; Hoelzel, M.; Holzapfel, M. Lithium Migration at High Temperatures in $Li_4Ti_5O_{12}$ Studied by Neutron Diffraction. *Chem. Mater.* **2011**, *23*, 2753−2759.